Supporting Information

Delley et al. 10.1073/pnas.1405314111

SI Text

General Considerations. All manipulations were performed under inert gas atmosphere using Schlenk techniques (Ar), glove box (Ar), and high-vacuum techniques (10^{-5} mbar). Benzene and tetrahydrofurano (THF) were dried over Na/benzophenone and distilled before use. Pentane was passed over two columns of activated alumina to dry and then degassed. Ethylene and propylene were passed through Cu-catalyst (R3-11 from BASF) and activated 4-Å molecular sieves before use. Elemental analyses were performed by the Mikroanalytisches Labor Pascher (Remagen, Germany). $NaOSi(O^tBu)_3$ was prepared according to ref. 1.

Preparation of $SiO_{2\text{-}(700)}$. Aerosil or Sylopol-948 was calcined at 500 °C (5 °C/min) for 4 h, treated at the same temperature for 12 h under a high vacuum (10^{-5} mbar), and then heated to 700 °C (5 °C/min) for 4 h under a high vacuum (10^{-5} mbar).

Sample Preparations. $SiO_{2\text{-}(700)}$ (1.00 g, 0.26 mmol surface SiOH) was suspended in a C_6H_6 (8 mL) solution of $[Cr(OSi(O^tBu)_3)_3(THF)_2]$ (265.2 mg, 0.32 mmol, 1.2 equivalents) at room temperature in an Ar-filled glovebox. The suspension was stirred at room temperature for 3 h, filtered, and washed with benzene (3 × 3 mL) and pentane (1 × 5 mL). Drying under a high vacuum (10^{-5} mbar) yields the blue $[(\equiv SiO)Cr(OSi(O^tBu)_3)_2(THF)]$. The combined C_6H_6 washings contained 0.10 mmol of $HOSi(O^tBu)_3$ that was quantified by ^1H NMR with a Cp_2Fe internal standard.

$[(\equiv SiO)Cr(OSi(O^tBu)_3)_2(THF)]$ (402.3 mg) was heated to 300 °C (5 °C/min) for 1 h and to 400 °C (5 °C/min) for 3 h under high-vacuum conditions (10^{-5} mbar) to yield blue $[(\equiv SiO)_3Cr]$. The volatiles released were analyzed by GC and GC-MS and by ^1H NMR with a Cp_2Fe as internal standard.

Poisoned samples were prepared by transferring a 4-picoline solution in pentane on a suspension of $[(\equiv SiO)_3Cr]$ in pentane. The reaction was stirred for 1 h at room temperature under reduced pressure. Nonadsorbed 4-picoline was recovered and quantified by GC-flame ionization detector, and the poisoned samples were dried at 10^{-5} mbar.

Infrared Spectroscopy. Infrared (IR) spectra were recorded in transmission mode on a Nicolet 6700 FT-IR spectrophotometer and on a Bruker Alpha transmission IR spectrometer.

Ultraviolet-Visible Spectroscopy. Ultraviolet-visible (UV-Vis) spectra were collected on an Agilent Technologies, Cary Series UV-Vis-NIR spectrophotometer in diffuse reflectance mode. The obtained reflectance spectra were converted into the corresponding absorbance spectra via their mathematical relation.

Electron Paramagnetic Resonance Spectroscopy. All measurements were conducted at X band [9.5-GHz electron paramagnetic resonance (EPR) frequency] on a Bruker EMX spectrometer, with a sample temperature of 110 K at a microwave power of 8 mW.

X-Ray Absorption Spectroscopy. X-ray absorption spectroscopy (XAS) at the Cr K-edge was measured at the SuperXAS beamline at the Swiss Light Source (SLS; Paul Scherrer Institute, Villigen, Switzerland). The SLS is a third-generation synchrotron operating at a 2.4-GeV electron energy and a current of 400 mA. The SuperXAS beamline is positioned on one of three superbent ports. The incident beam was collimated by a Si-coated mirror at 2.8 mrad, monochromatized using a double crystal Si(111) monochromator, and focused with an Rh-coated toroidal mirror (at 2.8 mrad) down to 100 × 100 μm with a beam intensity of 4–5 × 10^{11} ph/s. Calibration of the beamline energy was performed using Cr reference foil (Cr K-edge position at 5,989.0 eV). XAS transmission mode spectra were detected using ion chambers filled with He-N_2 gas mixtures; fluorescence spectra were measured using Silicon drift Ketek detector. Powder samples for fluorescence detection were filled in quartz capillaries (0.01 mm wall thickness, 0.9 mm outer diameter; Hilgenberg GmbH) under inert atmosphere, sealed with Apiezon vacuum grease and wax, and stored in glass tubes under argon that were opened just before the measurements. Multiple extended X-ray absorption fine structure (EXAFS) scans (5,900–6,800 eV) were averaged using new spots for each scan, with a scan time of ∼30 min. EXAFS data were analyzed using the Ifeffit program package (2). The EXAFS data were fitted in R-space (1–4 Å) after a Fourier transform (k = 1.5–10.5 $Å^{-1}$) using a k-weight of 2 for the molecular precursor and the grafted species and using a k-weight of 1, 2, and 3 for the thermally treated species.

Activity Measurements. Polymerization experiments were performed on the chromium catalyst supported on Sylopol-948 silica to prevent mass transfer limitations. A 500-mL glass reactor capped with a CaF_2 window for transmission infrared measurements and a side arm that was attached to a Teflon capped flask containing the chromium catalyst supported on Sylopol-948 silica (40 mg, 12 μmol Cr) was loaded in an Ar-filled glovebox. The inert atmosphere was removed and replaced with ethylene (∼300 mbar). The Teflon-capped flask containing the Cr catalyst was preheated to 70 °C for 5 min and then exposed to the ethylene atmosphere; this was taken as t = 0. Infrared spectra were acquired every 2 min, and the intensity of the band at 2,987 cm^{-1} was used to determine the pressure of ethylene at a given time.

Ethylene Polymerization at High Pressure. Ethylene polymerization were conducted in a fixed bed reactor using $[(\equiv SiO)_3Cr]$ (100 mg, 30 μmol Cr) mixed with dry NaCl (∼1 g) reacted with a gas mixture of ethylene (6 bar) and He (3 bar) at 70 °C for 75 s, as described previously (3).

The polymer produced at high ethylene pressure was characterized by high-temperature size exclusion chromatography (HT-SEC) and differential scanning calorimetry as described previously (3).

Computational Methods. All calculations were performed with the Gaussian09 program (4). Geometries were obtained by means of the hybrid B3LYP (5–9) functional in the doublet (S = 1/2) and quartet (S = 3/2) spin configuration of a d^3 Cr(III) ion and a combination of two different basis sets (BS1): LanL2DZ (10–12), a double-ξ valence basis set for Cr with the Hay and Wadt Effective Core Potential (ECP), and the 6-311G(*d*,*p*) (13, 14) basis set for all other atoms. The nature of all stationary points along the potential energy surfaces was confirmed by the computation of the Hessian matrix, obtaining no imaginary frequencies for minima and only one for transitions states structures. Intrinsic reaction coordinate (IRC) calculations were carried out only for transition states involved in the C–H bond activation steps to assure that the transition states connect properly reactants and products. Frequency calculations also allowed the computation of the gas phase corrections at 298.15 K and 1 atm to obtain zero-point energies and entropic contributions. Energetic refinement was carried out with a more extended basis set (BS2): LanL2TZ(*f*) (10, 15, 16) for Cr and 6-311++G(*d*,*p*) (13, 14, 17, 18) for all other atoms. Additionally, dispersion

corrections were calculated in a posteriori fashion on the B3LYP optimized geometries and added to the final energies by means of the DFT-D3 Grimme's methodology including Becke–Johnson (BJ) damping (19, 20) to obtain dispersion corrected Gibbs free energies: $\Delta G_{DFT\text{-}D3} = \Delta G_{KS\text{-}DFT} + \Delta E_{disp}$, where $\Delta G_{KS\text{-}DFT}$ is the Gibbs free energy obtained with any DFT functional and ΔE_{disp} is the dispersion correction.

Natural bond orbital calculations with the program NBO 5.9 of Weinhold and coworkers (21) were carried out at B3LYP level with the TZVP basis set (22, 23) on the B3LYP/BS1 optimized geometries.

To take into account some degree of anharmonicity in the analysis of CO adsorption, assuming that the anharmonicity is equal in free CO and in CO adsorbed on the surface, we corrected all CO frequencies with a scaling factor calculated as the ratio (0.988) between the experimental anharmonic (2,143 cm^{-1}) and the harmonic (2,170 cm^{-1}) frequency of the CO molecule.

1. McMullen AK, Tilley TD, Rheingold AL, Geib SJ (1989) Preparation and characterization of the monomeric copper(II) siloxide complex Cu[OSi(OCMe3)3]2(py)2. *Inorg Chem* 28(19): 3772–3774.
2. Ravel B, Newville M (2005) ATHENA, ARTEMIS, HEPHAESTUS: Data analysis for X-ray absorption spectroscopy using IFEFFIT. *J Synchrotron Radiat* 12(Pt 4):537–541.
3. Conley MP, et al. (2014) Polymerization of ethylene by silica-supported dinuclear Cr(III) sites through an initiation step involving C-H bond activation. *Angew Chem Int Ed Engl* 53(7):1872–1876.
4. Frisch MJ, et al. (2010) *Gaussian 09, Revision C.01* (Gaussian, Wallingford, CT).
5. Becke AD (1993) Density-functional thermochemistry. 3. The role of exact exchange. *J Chem Phys* 98(7):5648–5652.
6. Lee C, Yang W, Parr RG (1988) Development of the Colle-Salvetti correlation-energy formula into a functional of the electron density. *Phys Rev B Condens Matter* 37(2): 785–789.
7. Miehlich B, Savin A, Stoll H, Preuss H (1989) Results obtained with the correlation-energy density functionals of Becke and Lee, Yang and Parr. *Chem Phys Lett* 157(3): 200–206.
8. Stephens PJ, Devlin FJ, Chabalowski CF, Frisch MJ (1994) Ab-initio calculation of vibrational absorption and circular-dichroism spectra using density-functional force-fields. *J Phys Chem* 98(45):11623–11627.
9. Vosko SH, Wilk L, Nusair M (1980) Accurate spin-dependent electron liquid correlation energies for local spin-density calculations: A critical analysis. *Can J Phys* 58(8): 1200–1211.
10. Hay PJ, Wadt WR (1985) Abinitio effective core potentials for molecular calculations: Potentials for K to Au including the outermost core orbitals. *J Chem Phys* 82(1): 299–310.
11. Hay PJ, Wadt WR (1985) Abinitio effective core potentials for molecular calculations: Potentials for the transition-metal atoms Sc to Hg. *J Chem Phys* 82(1):270–283.
12. Wadt WR, Hay PJ (1985) Abinitio effective core potentials for molecular calculations: Potentials for main group elements Na to Bi. *J Chem Phys* 82(1):284–298.
13. Krishnan R, Binkley JS, Seeger R, Pople JA (1980) Self-consistent molecular-orbital methods. 20. Basis set for correlated wave-functions. *J Chem Phys* 72(1):650–654.
14. Mclean AD, Chandler GS (1980) Contracted Gaussian-basis sets for molecular calculations. 1. 2nd row atoms, Z=11-18. *J Chem Phys* 72(10):5639–5648.
15. Roy LE, Hay PJ, Martin RL (2008) Revised basis sets for the LANL effective core potentials. *J Chem Theory Comput* 4(7):1029–1031.
16. Ehlers AW, et al. (1993) A set of F-polarization functions for pseudo-potential basis sets of the transition metals Sc-Cu, Y-Ag and La-Au. *Chem Phys Lett* 208(1-2):111–114.
17. Frisch MJ, Pople JA, Binkley JS (1984) Self-consistent molecular-orbital methods. 25. Supplementary functions for Gaussian-basis sets. *J Chem Phys* 80(7):3265–3269.
18. Clark T, Chandrasekhar J, Spitznagel GW, Schleyer PV (1983) Efficient diffuse function-augmented basis sets for anion calculations. III. The 3-21+G basis set for first-row elements, Li-F. *J Comput Chem* 4(3):294–301.
19. Grimme S, Antony J, Ehrlich S, Krieg H (2010) A consistent and accurate ab initio parametrization of density functional dispersion correction (DFT-D) for the 94 elements H-Pu. *J Chem Phys* 132(15):154104.
20. Grimme S, Ehrlich S, Goerigk L (2011) Effect of the damping function in dispersion corrected density functional theory. *J Comput Chem* 32(7):1456–1465.
21. Glendening ED, et al. (2012) *NBO 5.9* (Theoretical Chemistry Institute, University of Wisconsin, Madison, WI).
22. Schafer A, Horn H, Ahlrichs R (1992) Fully optimized contracted Gaussian-basis sets for atoms Li to Kr. *J Chem Phys* 97(4):2571–2577.
23. Schafer A, Huber C, Ahlrichs R (1994) Fully optimized contracted Gaussian-basis sets of triple zeta valence quality for atoms Li to Kr. *J Chem Phys* 100(8):5829–5835.

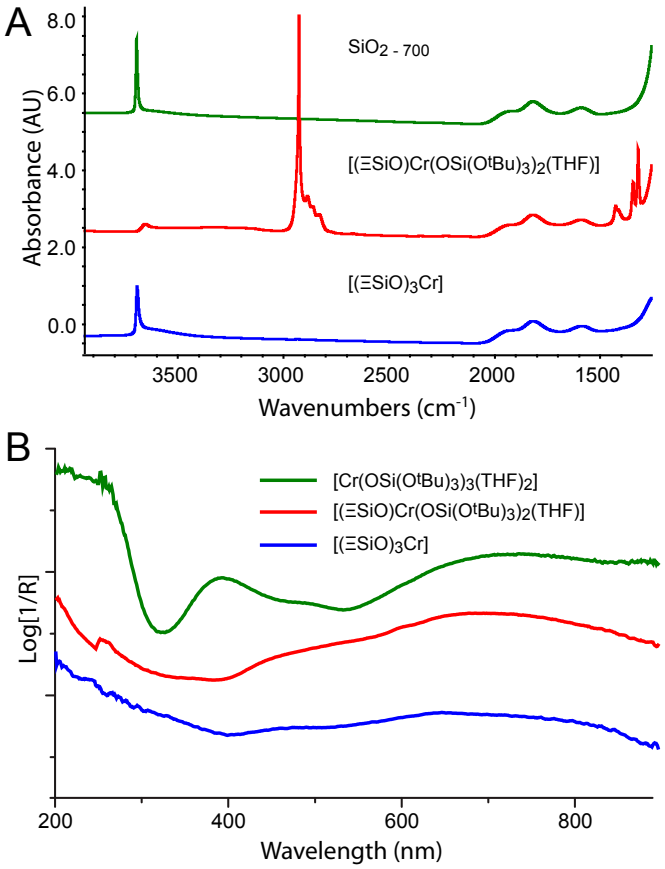

Fig. S1. (*A*) Infrared transmission spectrum SiO_{2-700} (green), [(≡SiO)Cr(OSi(O^{t}Bu)$_3$)$_2$(THF)] (red), and [(≡SiO)$_3$Cr] (blue). (*B*) UV-Vis absorbance spectra of Cr(OSi(O^{t}Bu)$_3$)$_3$(THF)$_2$ (green), [(≡SiO)Cr(OSi(O^{t}Bu)$_3$)$_2$(THF)] (red), and [(≡SiO)$_3$Cr] (blue). For clarity, the spectrum of [(≡SiO)$_3$Cr] has been zoomed in the *y* direction (ratio 1:2). The discontinuities and the increased noise level around 250 and 900 nm stem from instrumental artifacts.

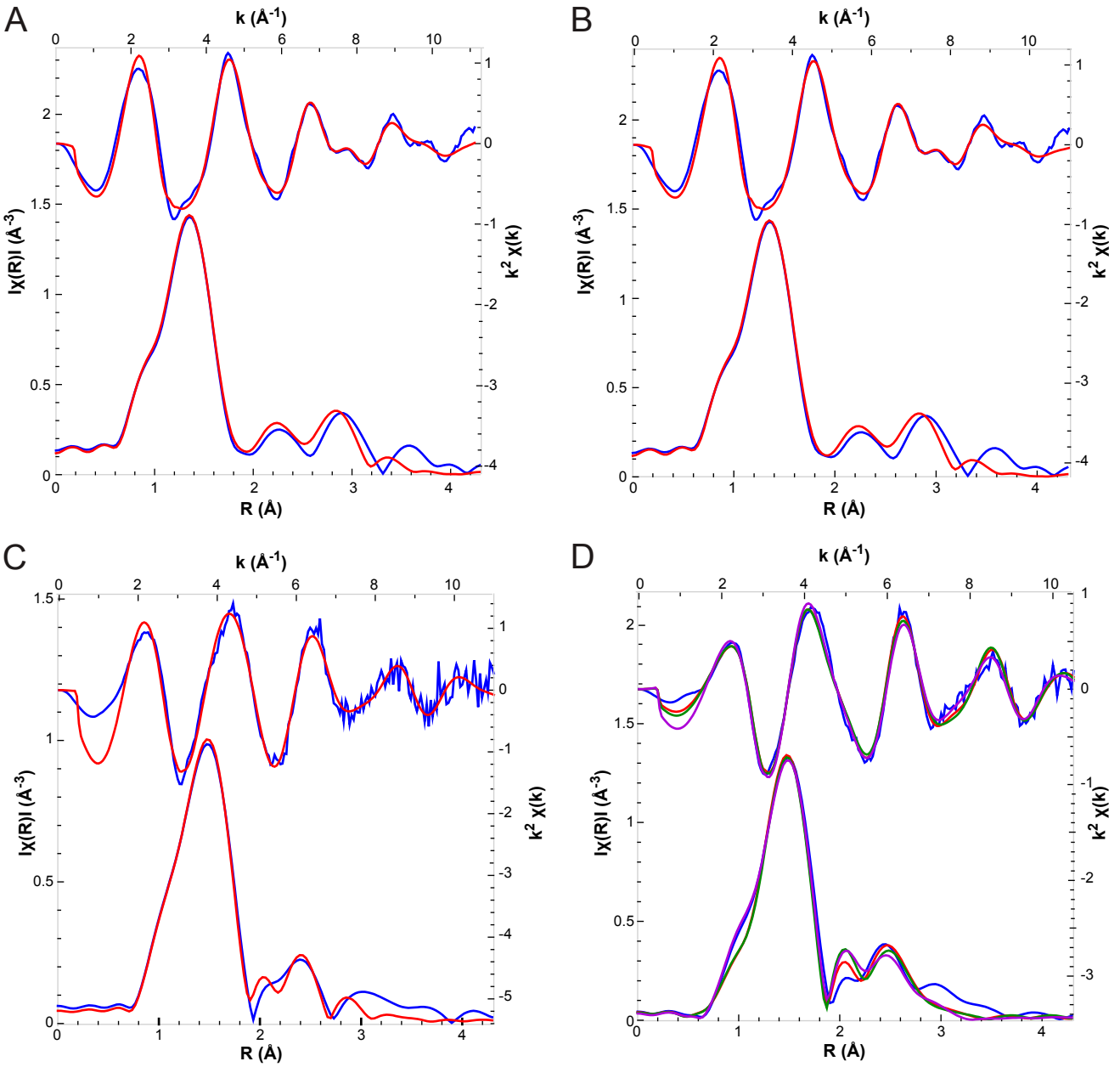

Fig. S2. Comparison of EXAFS data (blue) and fits (red) in k-space (*Upper*; top and right axes) and R-space (*Lower*; bottom and left axes). (*A*) $[Cr(OSi(O^tBu)_3)_3(THF)_2]$ using averaged paths, (*B*) $[Cr(OSi(O^tBu)_3)_3(THF)_2]$ using individual paths, (*C*) $[(\equiv SiO)Cr(OSi(O^tBu)_3)_2(THF)]$, and (*D*) $[(\equiv SiO)_3Cr]$ experimental data (blue) fits including a scattering path for 0 (green), 0.4 (red), and 1 (purple) additional oxygen atoms coordinated at longer distances.

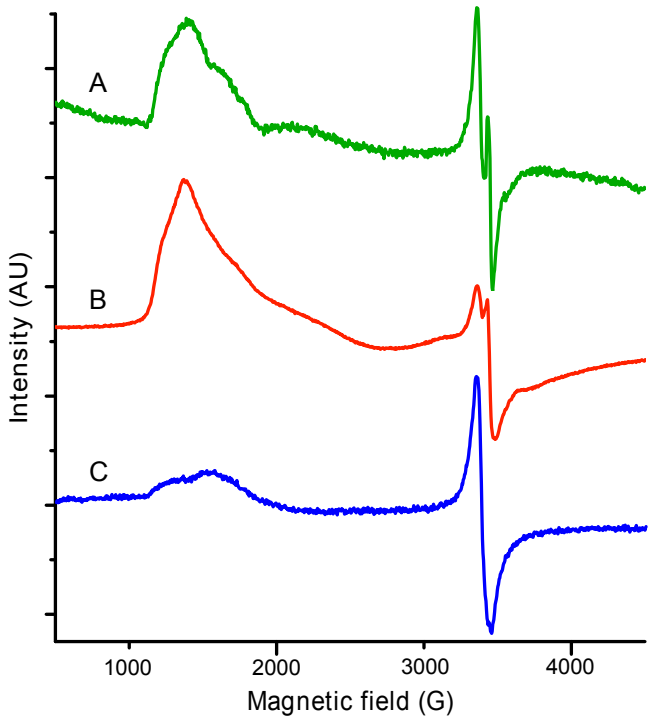

Fig. S3. EPR spectra of $[Cr(OSi(O^tBu)_3)_3(THF)_2]$ (**1**) (*A*), $[(\equiv SiO)Cr(OSi(O^tBu)_3)_2(THF)]$ (**2**) (*B*), and $[(\equiv SiO)_3Cr]$ (**3**) (*C*). All three spectra show a broad symmetric signal at approximately $g = 4.9$ (width, ~600 G) and a dispersive signal at approximately $g = 2.0$ (peak-to-peak width, ~200 G), consistent with an axial g-tensor. Note the sharp signal at $g = 2.0$ overlapping with previously mentioned dispersive signal for **1** and **2**, which is presumably due to the presence of trace organic based radical and which is not present for **3** after thermal treatment and loss of the organic ligands.

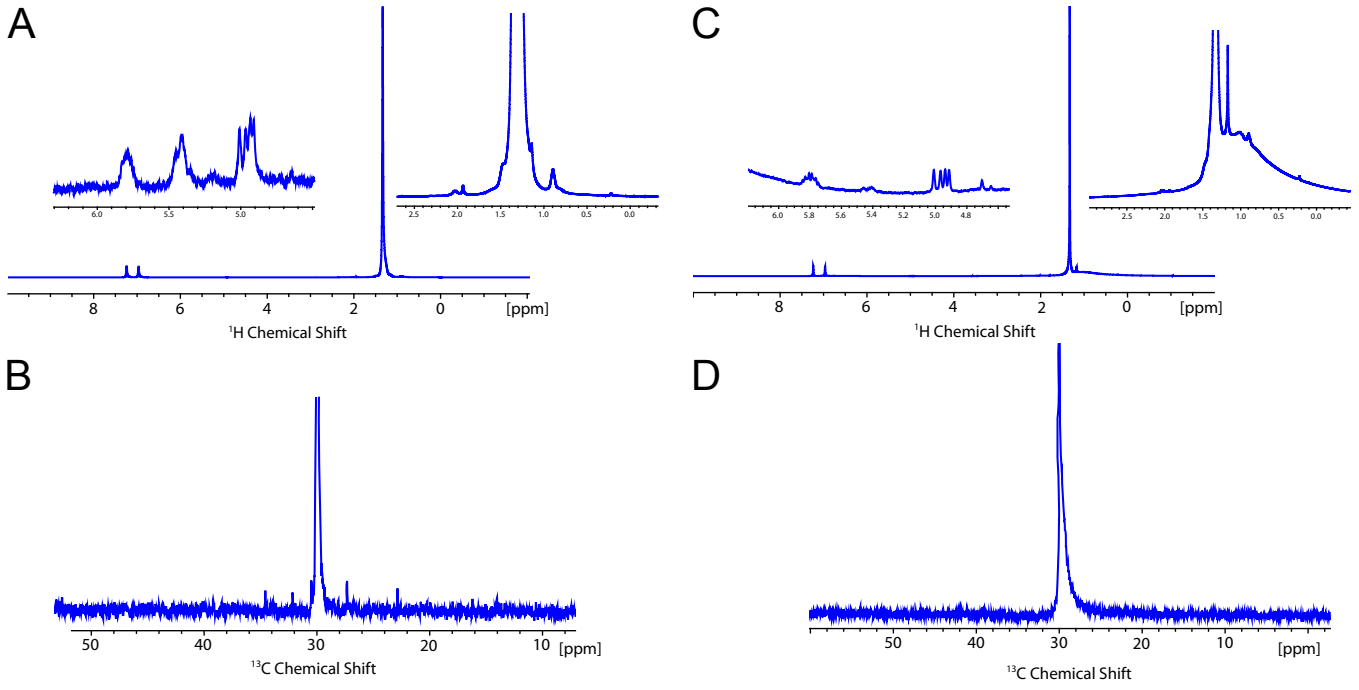

Fig. S4. ^{1}H (*A*) and ^{13}C NMR (*B*) of the polymers produced under low-pressure conditions and ^{1}H (*C*) and ^{13}C NMR (*D*) of the polymers produced under high-pressure conditions. All NMR measurements were performed at 120 °C, in d^4-1,2-dichlorobenzene, at 400 MHz.

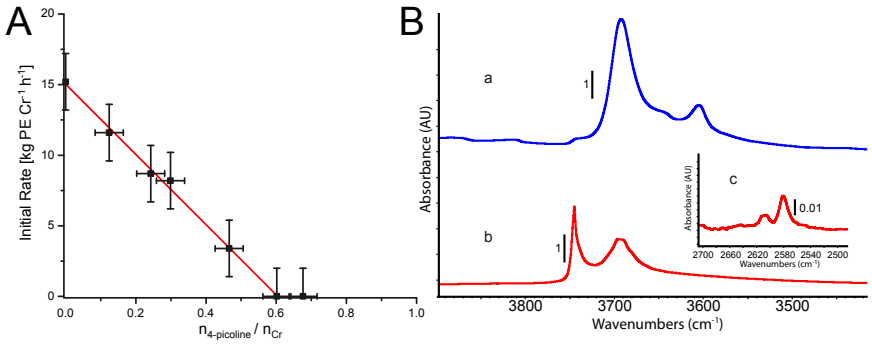

Fig. S5. (*A*) Initial rate of ethylene polymerization plotted against the degree of poisoning of [(≡SiO)$_3$Cr] with 4-picoline. (*B*) Transmission infrared spectra of [(≡SiO)$_3$Cr] treated with C_2H_4 (*a*) and C_2D_4 (*b*). *Inset* is (*c*) a zoom at 2,700–2,500 cm^{-1} of *b* showing a band at 2,581 and 2,609 cm^{-1}, which we assign to a Si–(μ-OD)–Cr(III) group and SiOD groups interacting with the polymer.

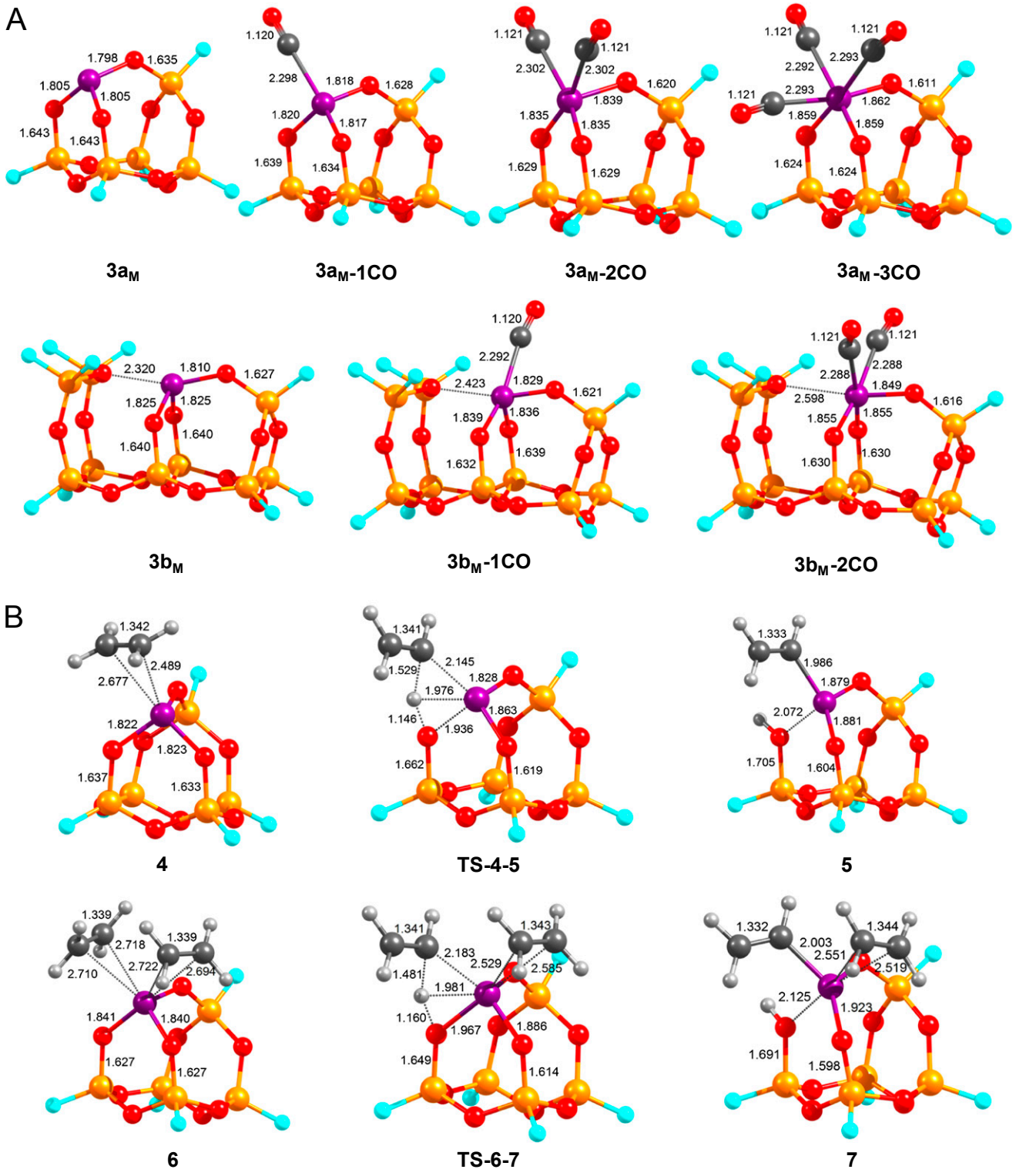

Fig. S6. (*A*) B3LYP/BS1 optimized structures of the carbonyl adducts of clusters $\mathbf{3a_M}$ and $\mathbf{3b_M}$. (*B*) B3LYP/BS1 optimized structures of the initiation pathways via C–H activation of ethylene with cluster $\mathbf{3b_M}$. Distances are given in Angstroms.

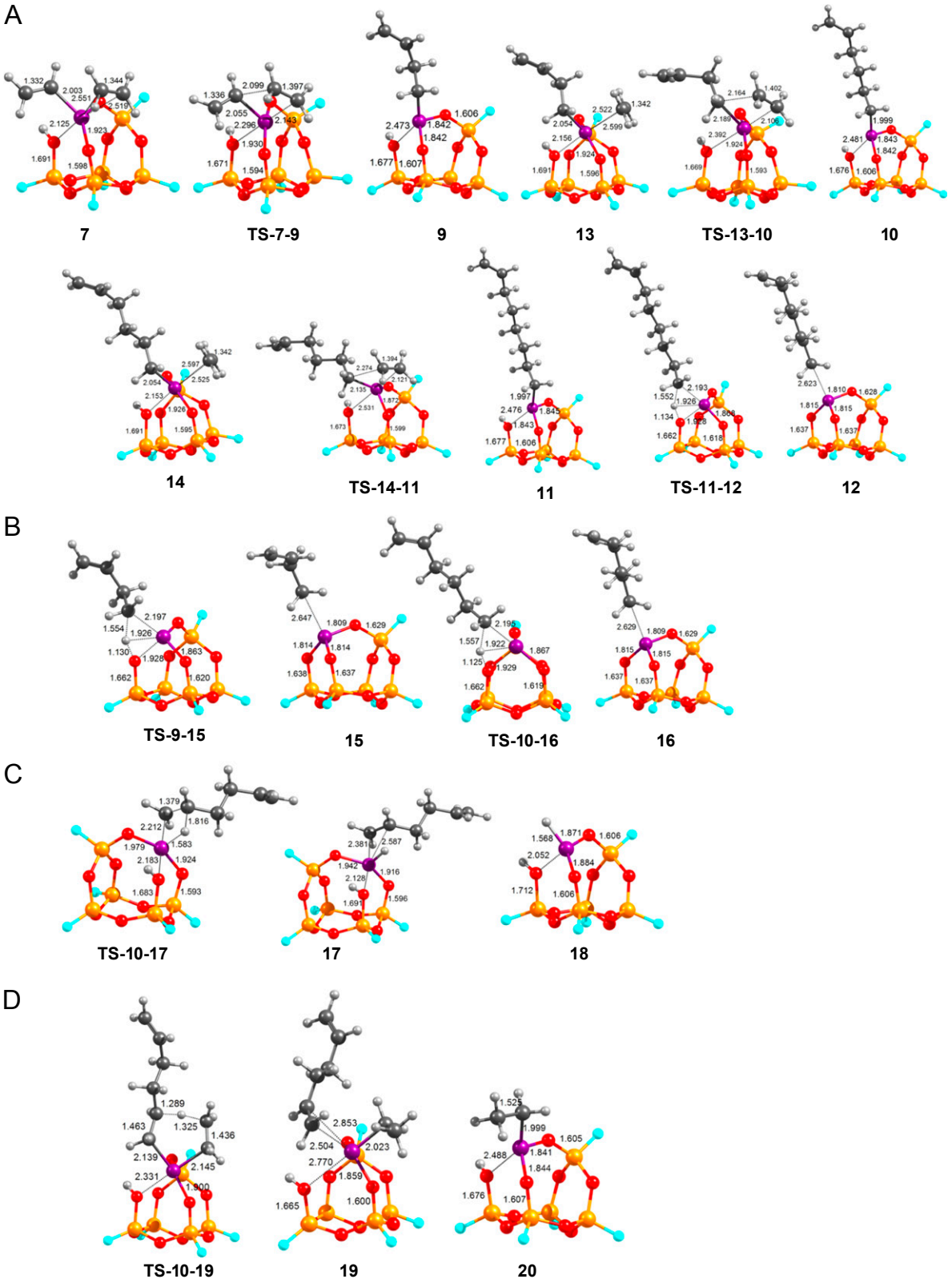

Fig. S7. B3LYP/BS1 optimized structures of the propagation and termination by H-transfer for the main catalytic cycle, as shown in Fig. 4 (*A*); termination by H-transfer from **9** and **11** (*B*); termination by β–H transfer (*C*); and termination by chain transfer to a monomer (*D*). Distances are given in Angstroms.

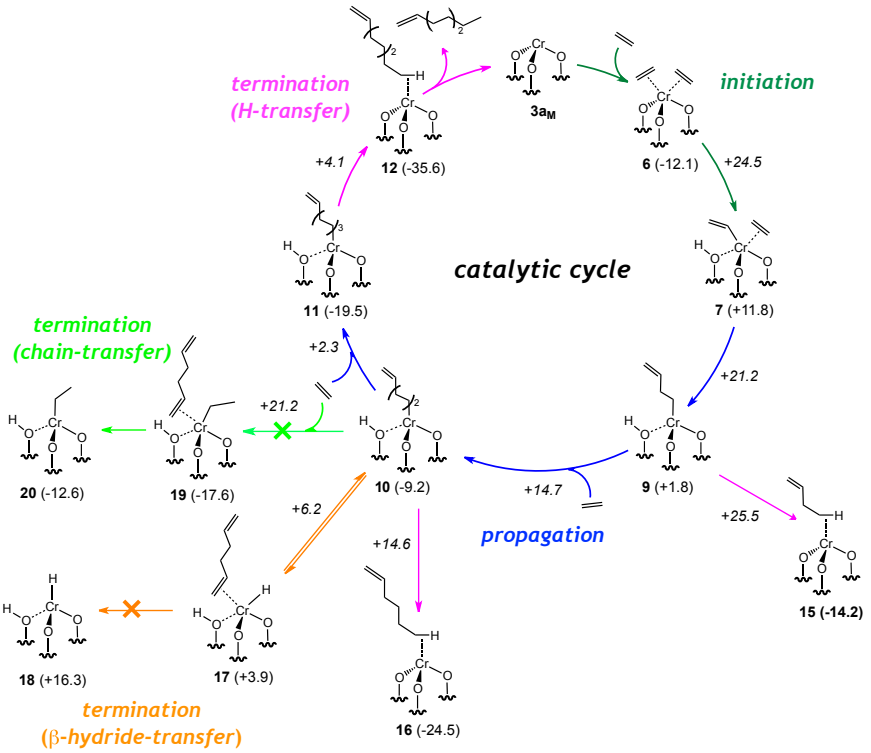

Fig. S8. DFT study of the ethylene polymerization mechanism, including alternative termination pathways. Numbers in parenthesis are Gibbs free energies of the corresponding intermediates and numbers in italic are Gibbs free energies of the corresponding transition states, normalized with respect to the system $\mathbf{3a_M}$ + 4 ethylene. All energies are in kcal/mol.

Table S1. EXAFS fits for $[Cr(OSi(O^tBu)_3)_3(THF)_2]$ (1) for averaged (entry 1) and individual scattering paths (entry 2), for $[(\equiv SiO)Cr(OSi(O^tBu)_3)_2(THF)]$ (2) (entry 3), and for $[(\equiv SiO)_3Cr]$ (3) including 0.4 (entry 4), 0 (entry 5), or 1 (entry 6) additional scattering paths for an oxygen at longer distances

Entry	Sample	χ^2_r*	Neighbor	N†	S02‡	r (Å)§	ΔE_0 (eV)¶	σ^2 (Å^2)‖
1	**1**	697	O	3	1	1.866 (5)	−1.0 (1.0)	0.0049 (9)
			O	2	1	2.018 (5)	−1.0 (1.0)	0.0049 (9)
			C	4	1	2.97 (1)	−1.0 (1.0)	0.010 (4)
			Si	3	1	3.553 (8)	−1.0 (1.0)	0.010 (3)
2	**1**	713	O	1	1	1.847 (5)	−1.0 (1.0)	0.0046 (9)
			O	1	1	1.856 (5)	−1.0 (1.0)	0.0046 (9)
			O	1	1	1.891 (5)	−1.0 (1.0)	0.0046 (9)
			O	1	1	2.008 (5)	−1.0 (1.0)	0.0046 (9)
			O	1	1	2.024 (5)	−1.0 (1.0)	0.0046 (9)
			C	1	1	2.93 (1)	−1.0 (1.0)	0.008 (4)
			C	1	1	2.96 (1)	−1.0 (1.0)	0.008 (4)
			C	1	1	2.97 (1)	−1.0 (1.0)	0.008 (4)
			C	1	1	3.06 (1)	−1.0 (1.0)	0.008 (4)
			Si	1	1	3.525 (8)	−1.0 (1.0)	0.009 (3)
			Si	1	1	3.533 (8)	−1.0 (1.0)	0.009 (3)
			Si	1	1	3.586 (8)	−1.0 (1.0)	0.009 (3)
3	**2**	20	O	3	1	1.95 (3)	−2 (1)	0.013 (3)
			O	1	1	2.00 (2)	−2 (1)	0.003 (2)
			C	2	1	3.02 (2)	−2 (1)	0.003 (2)
			Si	3	1	3.2 (1)	−2 (1)	0.05 (3)
4	**3**	146	O	3	1	1.973 (9)	−3.4 (9)	0.0027 (8)
			O	0.4	1	2.50 (6)	−3.4 (9)	0.0027 (8)
			Si	3	1	3.21 (2)	−3.4 (9)	0.009 (2)
5	**3**	1810	O	3	1	1.977 (10)	−2 (1)	0.0027 (8)
			O	0	—	—	—	—
			Si	3	1	3.22 (3)	−2 (1)	0.010 (3)
6	**3**	160	O	3	1	2.00 (1)	−4 (1)	0.002 (2)
			O	1	1	1.85 (4)	−4 (1)	0.002 (2)
			Si	3	1	3.20 (3)	−4 (1)	0.010 (3)

*Reduced χ^2 factor (normalized to degrees of freedom).
†N = coordination number.
‡S02 = amplitude.
§Distance of neighbor from Cr (SD in parentheses).
¶Energy shift.
‖Debye–Waller factor.